

The competition of electron and ion heating during magnetic reconnection

C. C. Haggerty,¹ M. A. Shay,¹ J. F. Drake,² T. D. Phan,³ C. T. McHugh¹

Corresponding author: Colby Haggerty, Bartol Research Institute, Department of Physics and Astronomy, University of Delaware, Newark, Delaware, USA (colbych@udel.edu)

¹Bartol Research Institute, Department of Physics and Astronomy, University of Delaware, Newark, DE 19716, USA

²Department of Physics and the Institute for Physical Science and Technology, University of Maryland, College Park, Maryland 20742, USA

³Space Sciences Laboratory, University of California, Berkeley, California 94720, USA

The physical processes that control the partition of released magnetic energy between electrons and ions during reconnection is explored through particle-in-cell simulations and analytical techniques. We demonstrate that the development of a large-scale parallel electric field and its associated potential controls the relative heating of electrons and ions. The potential develops to restrain heated exhaust electrons and enhances their heating by confining electrons in the region where magnetic energy is released. Simultaneously the potential slows ions entering the exhaust below the Alfvénic speed expected from the traditional counterstreaming picture of ion heating. Unexpectedly, the magnitude of the potential and therefore the relative partition of energy between electrons and ions is not a constant but rather depends on the upstream parameters and specifically the upstream electron normalized temperature (electron beta). These findings suggest that the fraction of magnetic energy converted into the total thermal energy may be independent of upstream parameters.

1. Introduction

Magnetic reconnection is a universal plasma process which converts stored magnetic energy into particle energy. The process is believed to be important in many astrophysical, solar, geophysical, and laboratory contexts. A principle topic in reconnection physics is the mechanism by which magnetic energy is partitioned into electron and ion thermal energy. A measure of this partition is the relative fraction of the available magnetic energy per particle $W = B_{rup}^2 / (4\pi m_i n_{up}) = m_i c_{Aup}^2$ (or its asymmetric generalization $m_i c_{A,asym}^2$ [Phan et al., 2013; Shay et al., 2014]) that goes to each class of particle; the supscript "up" denotes the upstream value and B_{rup} is the reconnecting component of the magnetic field.

Ion thermal energy often makes up a large fraction of the released magnetic energy during magnetic reconnection in both in the magnetosphere [Eastwood et al., 2013; Phan et al., 2014] and the laboratory [Yamada et al., 2014]. In the reconnection exhaust, where most magnetic energy is released, ion heating takes the form of interpenetrating beams [Cowley, 1982; Krauss-Varban and Omidi, 1995; Nakabayashi and Machida, 1997; Hoshino et al., 1998; Gosling et al., 2005; Lottermoser et al., 1998; Stark et al., 2005; Wygant et al., 2005; Phan et al., 2007], which are generated through Fermi reflection in the outflowing, contracting magnetic fields. The predicted counterstreaming velocity is twice the exhaust velocity c_{Aup} in the case of antiparallel reconnection even in the presence of Hall magnetic and electric fields [Drake et al., 2009]. The expected ion temperature increase based on such a simple picture is $\Delta T_i = 0.33 m_i c_{Aup}^2 = 0.33 W$. However, in solar wind and magnetopause observations the ion temperature increments are significantly lower than

expected, $\Delta T_i \sim 0.13 W$, but exhibit the expected scaling with parameters [*Drake et al.*, 2009; *Phan et al.*, 2014].

The scaling of electron heating is much more challenging to understand because the single-pass Fermi reflection yields only a small increase in the electron temperature. Nevertheless, magnetopause observations for electrons yield a similar scaling $\Delta T_e \sim 0.017 W$ although with significantly less heating compared to the ions [*Phan et al.*, 2013]. Simulations also yield this scaling [*Shay et al.*, 2014] although the electron heating mechanism remains under debate [*Haggerty et al.*, 2014; *Egedal et al.*, 2015].

Thus, it is important not only to establish the explicit mechanisms for electron and ion heating during reconnection but also to determine whether the partition of energy between the two species is a universal relation or varies with parameters. We demonstrate here through a set of comprehensive computer simulations and analytic methods that the large-scale parallel potential that develops within the reconnection exhaust controls and links together both electron and ion heating and regulates the partition of released magnetic energy. The development of this potential within the exhaust to prevent the escape of hot electrons has been well-established [*Egedal et al.*, 2008] and enables electrons to undergo repeated Fermi reflections within the reconnection exhaust. In the present paper we identify the mechanism that ultimately limits electron energy gain. The spatial variation of the potential propagates outward from the exhaust as a component of a slow shock [*Liu et al.*, 2012]. The electron temperature and the associated shock velocity increase until the velocity matches that of the Alfvénic exhaust. At this point electron energy gain through Fermi reflection ends since the bounce length of electrons trapped in the exhaust no longer

decreases with time as they propagate downstream. At the same time that the potential serves to facilitate electron energy gain, it suppresses ion heating: the parallel streaming velocity of ions injected into the exhaust from upstream is reduced below the Alfvén speed by the potential so that the counterstreaming velocity of ions is less than $2c_{Aup}$. Thus, the strength of the potential regulates the relative heating of electrons and ions. We show that the potential increases with increasing upstream electron temperature T_{eup} and that ΔT_e can actually exceed ΔT_i – the partition of electron and ion heating measured in the magnetosphere [Eastwood *et al.*, 2013; Phan *et al.*, 2013, 2014] and laboratory experiments [Yamada *et al.*, 2014] is not universal. However, the total heating is unaffected by the potential and the fraction of magnetic energy converted into thermal energy is constant for the simulations performed, with $\Delta(T_i + T_e) \approx 0.15 m_i c_{Aup}^2 = 0.15 W$. Remarkably, despite the numerous differences between the simulations and observations, this slope is the same as the Phan *et al.* [2013, 2014] measurement of total heating at the Earth’s magnetopause.

2. Simulations:

We use the PIC code P3D[Zeiler *et al.*, 2002] to perform simulations in 2.5 dimensions of collisionless antiparallel (no guide field) reconnection. Magnetic field strengths and particle number densities are normalized to B_0 and n_0 , respectively. Lengths are normalized to the ion inertial length $d_{i0} = c/\omega_{pi0}$ at the reference density n_0 , time to the ion cyclotron time $\Omega_{ci0}^{-1} = (eB_0/m_i c)^{-1}$, and velocities to the Alfvén speed $c_{A0} = \sqrt{B_0^2/(4\pi m_i n_0)}$. Electric fields and temperatures are normalized to $E_0 = c_{A0}B_0/c$ and $T_0 = m_i c_{A0}^2$, respectively. In the simulation coordinate system the reconnection outflows are along \hat{x} and the

inflows are along \hat{y} . Simulations are performed in a periodic domain with a system size of $L_x \times L_y = 204.8 d_{i0} \times 102.4 d_{i0}$, and 100 particles per grid in the inflow region. Simulation parameters, which are given in the table in the Supplementary Material, included ion-to-electron mass-ratios of 25 and 100 and a variety of upstream initial temperatures and magnetic fields. The initial conditions are a double current sheet [Shay *et al.*, 2007].

A small magnetic perturbation is used to initiate reconnection. Each simulation is evolved until reconnection reaches a steady state, and then for analysis purposes during this steady period the simulation data is time averaged over 100 particle time steps, which is typically on the order of 50 electron plasma wave periods ω_{pe}^{-1} .

3. Overview of electron and ion heating:

We first present an overview of electron and ion heating as measured in the simulations. The temperature of electrons and ions each increase with the distance downstream of the x-line in the exhaust until it approaches a constant. This behavior has already been discussed in detail for electrons [Shay *et al.*, 2014] and is discussed more fully in the Supplementary Material for the ions. To determine ΔT_i and ΔT_e in a given simulation we average T_i and T_e over a region downstream and then subtract the inflow temperature. Details of how this average is computed for ions are found in the Supplementary Material. In Fig. 1 we present an overview of (a) electron, (b) ion and (c) the total temperature increments versus $m_i c_{Aup}^2$. The red triangles correspond to high upstream electron temperature $T_e/T_i = 9$. As expected, the sum of the electron and ion heating increments scale with the available magnetic energy per particle with an approximate slope of $\Delta(T_i + T_e) \approx 0.15 m_i c_{Aup}^2 = 0.15 W$. This slope is the same as measured in

observations of electron and ion heating in reconnection exhausts at the Earth's magnetopause [Phan *et al.*, 2013, 2014]. Surprisingly, however, the individual electron and ion temperature increments in Fig. 1 have a larger spread related to the upstream electron temperature. The electron heating is generally significantly below that of the ions, as in the observational data [Phan *et al.*, 2013]. The exceptions are the runs with high electron temperature upstream, which produce enhanced electron heating and reduced ion heating with the electron heating significantly greater than the ion heating. These simulations therefore demonstrate the parameter-dependence of energy partition between electrons and ions. In the remainder of the manuscript we explore the mechanisms that control the heating of both species, starting with the ions.

Shown in Figs. 2a-c are the ion parallel temperature $T_{i\parallel}$, perpendicular temperature $T_{i\perp}$ and total temperature ($T_i \equiv [T_{i\parallel} + 2T_{i\perp}] / 3$). Downstream of the x-line $T_{i\parallel}$ increases and broadens in the inflow direction to fill the exhaust. The band of $T_{i\perp}$ at the midplane of the exhaust is produced by the Speiser orbits of the ions [Speiser, 1965; Drake *et al.*, 2009]. As with the electrons, the total ion temperature asymptotes to a constant downstream [Shay *et al.*, 2014]. The underlying mechanism for ion heating well downstream of the x-line was outlined by Drake *et al.* [2009]. In this downstream region, $\mathbf{E}_{\perp} = 0$ in the reference frame moving with the reconnected magnetic field lines. This includes both the reconnecting and Hall electric fields as shown in Fig. 3 of Drake *et al.* [2009]. Within the ion diffusion region, however, the strong normal electric field cannot be transformed away [Wygant *et al.*, 2005]. In this moving frame the cold ion population enters the reconnection exhaust with a parallel velocity equal to the field line velocity v_0 . The ions reach the midplane,

undergo an energy-conserving reflection, and then travel back out along the field line. The reflected population mixes with cold incoming ions creating counter-streaming beams and a temperature increment of $\Delta T_i \approx \Delta T_{i\parallel}/3 \approx m_i v_0^2/3$. In order to test this prediction we directly measure the field line velocity $v_0 \approx -c E_z/B_y$, which asymptotes to the ion outflow velocity v_{ix} in the downstream region. The prediction of $\Delta T_i = m_i v_0^2/3$ is tested in Fig. 3a. The points roughly scale with $m_i v_0^2/3$, but there are two significant differences relative to the theoretical value: (1) There are outlier points leading to a large spread of the data, and (2) all of the data points are substantially below the theoretical prediction (line of slope = 1 as indicated by the dashed black line). In Fig. 3b, examination of the ion distribution function integrated along v_z around $(X, Y) = (190, 25.6)$ reveals that the beaming velocities are significantly less than v_0 . The magnetic field points along \hat{y} , and two field-aligned counterstreaming populations straddle $v_y = 0$ but well within the region $|v_y/v_0| < 1$.

We now show that the reduction in ion heating is a consequence of the large-scale potential that confines the hot electrons (see cuts of $T_{e\parallel}$ and n in Fig. 2e) in the exhaust. In order to maintain electron force balance along the magnetic field, a large-scale, although relatively small magnitude, parallel electric field arises (Fig. 2d). The E_{\parallel} fills the exhaust and points away from the midplane. This electric field and associated potential slows down inflowing ions leading to a reduced ion beam velocity and a reduced ΔT_i .

Note that in Fig. 2d there is an inverted E_{\parallel} structure straddling the midplane that is not to be confused with the larger scale parallel field discussed above. This smaller scale parallel electric field is connected with the outer electron diffusion region associated with

the super-Alfvénic electron jet [*Shay et al.*, 2007], and does not couple to the ions, which are unmagnetized at these small scales. For that reason, the effect of this electron scale parallel electric field is not included in our analysis.

To calculate the impact of the large scale parallel electric field and the associated potential on the ions, it is necessary to understand both its amplitude and space-time structure. The spatial variation of the potential propagates as a component of the exhaust boundary moving outward away from the midplane. This exhaust boundary takes the form of super-slow to sub-slow transition rather than a switch-off shock because of the strong temperature anisotropy that develops in collisionless reconnection [*Liu et al.*, 2012]. We determine this velocity directly from the simulation by calculating the potential ϕ by integrating E_{\parallel} along the magnetic field. We take $\phi = 0$ at the X value of the middle of the island ($X = 256.4$), where the distance along the field line l is also taken to be zero. In Fig. 4a we plot ϕ versus l and the X -intercept of the field line with the midplane of the exhaust, denoted as X_{int} . Only the portion above the exhaust midplane is shown so that the expansion of the white zone with distance downstream measures the rate of shortening of the field line (using the time axis which is defined by $\Delta t = \Delta X/v_0$). The boundary of the white zone parallels the solid line in the white zone, which marks the exhaust velocity v_0 , so field line shortening is at the velocity v_0 as expected. The more important result of Fig. 4 is that the contours of ϕ parallel the boundary of the white zone which means that the expansion velocity of the potential is v_0 , the same as the shortening rate of the field lines. This is a crucial result that will enable us to explicitly calculate ion heating and impose limits on electron heating.

We analytically calculate the magnitude of ϕ from the parallel electric field, which follows from electron force balance:

$$eE_{\parallel} = -\nabla_b T_{e\parallel} - T_{e\parallel} \nabla_b \ln n + (T_{e\parallel} - T_{e\perp}) \nabla_b \ln B, \quad (1)$$

where $\nabla_b = (\mathbf{B}/B) \cdot \nabla$. The potential ϕ , is then given by $\phi \equiv -\int E_{\parallel} dl$. Integrating Eq. 1 and multiply both side by -1 yields $\phi = \phi_{Te} + \phi_n + \phi_B$, where the subscript represents the quantity acted on by the gradient, i.e.,

$$\phi_n \equiv \int (T_{e\parallel}/e) (\nabla_b \ln n) dl. \quad (2)$$

In Fig. 4b, these potentials are plotted along the solid black field line shown in Fig. 2d. ϕ_{Te} , ϕ_n , and ϕ_B have different constants added to aid in their comparison with ϕ . ϕ increases from the inflow region to the exhaust, reaching its maximum value just outside the midplane. We have found through test particle simulations that as the ions enter the exhaust only ϕ_n significantly modifies the ion beam velocity (and therefore ΔT_i). ϕ_B is small. ϕ_{Te} is significant in a narrow region at the edge of the exhaust but because it is so localized and because there is a large transverse electric field in this region, test particle trajectories provided in the supplementary material reveal that the ions cross this region transverse to \mathbf{B} and don't respond to ϕ_{Te} . The dip in ϕ at the midplane of the exhaust is similarly unimportant since it only affects the ion temperature within a narrow region that occupies a decreasingly small fraction of the exhaust with distance downstream.

Thus, ϕ_n has the greatest impact on ΔT_i . To calculate ΔT_i we therefore need to evaluate the jump in ϕ_n across the exhaust. Since $T_{e\parallel}$ is nearly constant across the exhaust (Fig. 2e) we can replace it by its average value $T_{e\parallel d}$ in the integral in Eq. 2. The density varies from a minimum n_{min} at the exhaust boundary to a maximum n_d in the middle of the

exhaust so the jump in ϕ_n across the exhaust $\Delta\phi_n$ is given by

$$e\Delta\phi_n \approx T_{e\parallel d} \ln(n_d/n_{min}). \quad (3)$$

The jump $\Delta\phi_n$ is marked in the simulation data in Fig. 4b. In Fig. 4c we plot the value of $\Delta\phi_n$ measured from the simulation against the values from Eq. 3. The agreement is excellent. Note the large value of the potential for the simulations with high value of upstream T_e/T_i (red triangles). We can now extend the model of *Drake et al.* [2009] to include the effect of ϕ_n to obtain a more accurate ion heating prediction. In a frame moving with the field line the potential is also unchanging since its outflow velocity is also v_0 . In this frame the incoming population will be slowed down from the field line velocity (v_0) to the exhaust beam velocity (v_d). These slower ions mix with incoming ions from the other side of the midplane, leading to counterstreaming beams and a temperature increment of $\Delta T_i = m_i v_d^2/3$. In the frame of the potential the ion energy is conserved so we can calculate v_d directly from $\frac{1}{2} m_i v_0^2 - e\Delta\phi_n = \frac{1}{2} m_i v_d^2$. Solving for v_d and substituting in ΔT_i , we find

$$\Delta T_i = \frac{m_i v_0^2}{3} \left(1 - \frac{2e\Delta\phi_n}{m_i v_0^2} \right) \quad (4)$$

In Fig. 4d we insert the measured $\Delta\phi_n$ from the simulation in Eq. 4 and compare the prediction with the measured ion heating in the simulations. The spread in the data is markedly reduced compared with that in Fig. 3a: all of the points now straddle a line with a slope of 1. Most revealing is the change in position of the $T_e/T_i = 9$ simulations which are denoted by red triangles in Figs. 3 and 4. These simulations have large $\Delta\phi_n$ which significantly reduces the ion beam velocity and the corresponding ion temperature

increment. Thus, electrons, through the self-generated potential have a strong impact on ion heating.

A question remains as to why previous observational studies measure an ion increment $\Delta T_i \propto m_i v_0^2$ [Drake *et al.*, 2009; Phan *et al.*, 2014], even though such a scaling is not implied by Eq. 4 due to the presence of the potential $\Delta\phi_n$. $\Delta\phi_n$ depends on both $\Delta T_{e\parallel}$, and T_{eup} in Eq. 2; the logarithm of the density compression ratio is not expected to vary significantly with upstream conditions for symmetric reconnection. For a significant variation of upstream properties, $\Delta T_{e\parallel}$ has been shown to scale with $m_i v_0^2 \approx m_i c_{Aup}^2$ [Phan *et al.*, 2013; Shay *et al.*, 2014]. Any deviation from the $m_i v_0^2$ scaling, therefore, is linked to $T_{eup}/(m_i c_{Aup}^2) \approx \beta_{eup}/2$. As long as the electron heating is sufficiently strong compared to the upstream temperature, ΔT_e should dominate, and we recover both the observational scaling and the scaling of the black triangles in Fig. 3a.

Since weak parallel electric fields are impossible to directly measure with in situ satellite measurements, the analytic expression for $e\Delta\phi_n$ in Eq. 3 can be used to evaluate ΔT_i in Eq. 4 to compare with observations. In addition, the prediction can be further simplified by using the approximation $v_0 \approx c_{Aup}$.

We now discuss the impact of the potential on electron heating. It has been shown that the dominant driver of electron heating during anti-parallel reconnection is Fermi reflection [Dahlin *et al.*, 2014]. In the absence of scattering, electron energy gain is mostly along the local magnetic field. On the other hand, a single Fermi reflection of electrons in the reconnection exhaust is not sufficient to drive significant electron energy gain. Electrons can gain energy through multiple Fermi reflections during multi x-line reconnection [Drake

et al., 2006; *Oka et al.*, 2010; *Drake et al.*, 2013] or in a single x-line reconnection as a result of the potential ϕ , which acts to confine electrons within the reconnection exhaust [*Egedal et al.*, 2008]. What limits the electron temperature within the exhaust $T_{ed\parallel}$ and therefore the potential (Eq. 2) has not been established. Electrons can continue to gain energy in a single exhaust by repeatedly reflecting off of the potential to return to the exhaust core for additional Fermi reflections. This behavior is shown by the test particle trajectory in Fig 3c, and it is shown in the supplemental material that the reflection is due primarily to the potential and not to mirroring. However, electrons lose energy in their reflection from the potential (in the frame of the x-line) since the potential is moving outward along the magnetic field. The energy gain from Fermi reflection continues to exceed the loss from reflection from the potential as long as the expansion velocity is less than v_0 , the field line velocity. Thus, Fig. 4a, which demonstrates that the expansion velocity and field line velocity converge downstream, establishes how electron energy gain is limited. The shock bounding the reconnection exhaust, as discussed by *Liu et al.* [2012], carries the potential outward along \mathbf{B} . The electron temperature increases, increasing the shock velocity, until the shock speed reaches v_0 and electron heating saturates.

Here we do not present a complete model of the electron heating during reconnection, which requires a full understanding of the dependence of the shock velocity on electron and ion temperatures upstream and downstream. Instead we simply note that in the limit of low upstream pressure (high upstream mach number) the propagation speed of a simple parallel propagating slow shock with a jump in the parallel temperature is $2\sqrt{\Delta(T_e + T_i)/m_i}$. Equating this speed to $v_0 = c_{Aup}$, we find $\Delta(T_e + T_i) = 0.25 m_i c_{Aup}^2 =$

$0.25 W$, which is within a factor of two of the simulation and observational findings of $0.15 W$ [Phan *et al.*, 2013, 2014]. There is significant uncertainty in the 0.25 coefficient, however, due to the simplistic nature of the shock analysis used to derive it. Nevertheless, the basic idea that the electron and ion temperature increments are linked through their control of the propagation speed of the shock and associated potential is consistent with the results of Fig. 1c.

4. Conclusions:

We present the results of PIC simulations of reconnection-driven electron and ion heating that suggest that the partition of energy gain of the two species is controlled by the large-scale potential that develops to prevent hot electrons in the reconnection exhaust from escaping along open magnetic field lines. We first show that the relative heating of electrons and ions is controlled by the relative magnitudes of the upstream temperatures of each species – high upstream electron temperature yields much higher electron than ion heating demonstrating that the typical partition of energy seen in space and the laboratory are not universal. We then carry out a detailed study of ion heating and show that the potential slows ions injected into the exhaust to values below the Alfvénic exhaust flow speed. Ion heating therefore can fall well below the characteristic value $\Delta T_i = m_i v_0^2/3$ predicted by simple Fermi reflection. The scaling of ΔT_i in the simulations is consistent with this theory. The suppression of ion heating becomes very significant for high upstream electron temperature when the potential becomes very large. The mechanism by which the potential controls electron heating is also discussed. The potential confines electrons within the exhaust and enables them to undergo multiple Fermi reflections. The

outward propagation of the spatial variation of the confining potential, which is linked to the slow shock that bounds the exhaust, ultimately halts electron energy gain when its velocity reaches the exhaust velocity – energy gain through Fermi reflection then balances energy loss through reflection off the outward propagating potential. Thus, the electron temperature rises until the shock/potential velocity matches the exhaust velocity. The potential is therefore the key ingredient that controls both electron and ion heating and their relative energy gain.

An intriguing result is that the total plasma heating ($\Delta T_{tot} = \Delta T_e + \Delta T_i$) in the simulations is constant with $\Delta T_{tot} \approx .15 W$, which is consistent with recent magnetospheric observations [*Phan et al.*, 2013, 2014]. Although this is an exciting result, our simulations explore only the small parameter regime of symmetric and anti-parallel reconnection. Determination of the generality of the ΔT_{tot} scaling will require a more systematic scaling study. Regarding the comparison with satellite observations: On the one hand the fact that the observations are of asymmetric reconnection and the simulations are symmetric requires some caution during comparison; Clearly, the simulation scaling study should be extended to asymmetric reconnection. On the other hand, the fact that asymmetric observations have such good agreement with symmetric simulations implies that the scaling may be a general result, applicable to a wide range of reconnecting systems.

Acknowledgments. This research was support by the NASA Space Grant program at the University of Delaware; NSF Grants Nos. AGS-1219382 (M.A.S) and AGS-1202330 (J. F. D); NASA Grants Nos. NNX08A083G–MMS IDS (T.D.P and M.A.S), NNX14AC78G (J.F.D), NNX13AD72G (M.A.S.), and NNX15AW58G (M.A.S). Simulations and anal-

ysis were performed at the National Center for Atmospheric Research Computational and Information System Laboratory (NCAR-CISL) and at the National Energy Research Scientific Computing Center (NERSC). We wish to acknowledge support from the International Space Science Institute in Bern, Switzerland.

References

- Cowley, S. W. H. (1982), The causes of convection in the earth's magnetosphere - A review of developments during the IMS, *Reviews of Geophysics and Space Physics*, *20*, 531–565, doi:10.1029/RG020i003p00531.
- Dahlin, J. T., J. F. Drake, and M. Swisdak (2014), The Mechanisms of Electron Heating and Acceleration during Magnetic Reconnection, *Phys. Plasmas*, *21*, 092,304, doi:doi:10.1063/1.4894484.
- Drake, J. F., M. Swisdak, K. M. Schoeffler, B. N. Rogers, and S. Kobayashi (2006), Formation of secondary islands during magnetic reconnection, *Geophys. Res. Lett.*, *33*, L13,105, doi:10.1029/2006GL025957.
- Drake, J. F., M. Swisdak, T. D. Phan, P. A. Cassak, M. A. Shay, S. T. Lepri, R. P. Lin, E. Quataert, and T. H. Zurbuchen (2009), Ion heating resulting from pickup in magnetic reconnection exhausts, *J. Geophys. Res.*, *114*, A05111, doi:10.1029/2008JA013701.
- Drake, J. F., M. Swisdak, and R. Fermo (2013), The Power-law Spectra of Energetic Particles during Multi-island Magnetic Reconnection, *ApJ Lett.*, *763*, L5, doi:10.1088/2041-8205/763/1/L5.
- Eastwood, J. P., T. D. Phan, J. F. Drake, M. A. Shay, A. L. Borg, B. Lavraud, and M. G. G. T. Taylor (2013), Energy Partition in Magnetic Reconnection in Earth's

- Magnetotail, *Phys. Rev. Lett.*, *110*(22), 225001, doi:10.1103/PhysRevLett.110.225001.
- Egedal, J., W. Fox, N. Katz, M. Porkolab, M. Øieroset, R. P. Lin, W. Daughton, and J. F. Drake (2008), Evidence and theory for trapped electrons in guide field magnetotail reconnection, *Journal of Geophysical Research (Space Physics)*, *113*(12), A12207, doi:10.1029/2008JA013520.
- Egedal, J., W. Daughton, A. Le, and A. L. Borg (2015), Double layer electric fields aiding the production of energetic flat-top distributions and superthermal electrons within the exhausts from magnetic reconnection, *ArXiv e-prints*.
- Gosling, J. T., R. M. Skoug, D. J. McComas, and C. W. Smith (2005), Direct evidence for magnetic reconnection in the solar wind near 1 AU, *J. Geophys. Res.*, *110*(A9), 1107–+, doi:10.1029/2004JA010809.
- Haggerty, C. C., M. A. Shay, J. F. Drake, T. D. Phan, P. Wu, and M. M. Swisdak (2014), Electron Heating During Magnetic Reconnection: The Interplay of Parallel Electric Fields and Fermi-Bounce Acceleration, *AGU Fall Meeting Abstracts*, p. A4152.
- Hoshino, M., T. Mukai, T. Yamamoto, and S. Kokubun (1998), Ion dynamics in magnetic reconnection: Comparison between numerical simulation and Geotail observations, *J. Geophys. Res.*, *103*, 4509–4530, doi:10.1029/97JA01785.
- Krauss-Varban, D., and N. Omidi (1995), Large-scale hybrid simulations of the magnetotail during reconnection, *Geophys. Res. Lett.*, *22*(23), 3271–3274.
- Liu, Y.-H., J. F. Drake, and M. Swisdak (2012), The structure of the magnetic reconnection exhaust boundary, *Phys. Plasmas*, *19*, 022,110.

- Lottermoser, R. F., M. Scholer, and A. P. Mathews (1998), Ion kinetic effects in magnetic reconnection, *J. Geophys. Res.*, *103*, 4547.
- Nakabayashi, J., and S. Machida (1997), Electromagnetic hybrid-code simulation of magnetic reconnection: Velocity distribution functions of accelerated ions, *Geophys. Res. Lett.*, *24*, 1339–1342, doi:10.1029/97GL01206.
- Oka, M., T.-D. Phan, S. Krucker, M. Fujimoto, and I. Shinohara (2010), Electron Acceleration by Multi-Island Coalescence, *Astrophys. J.*, *714*, 915–926, doi:10.1088/0004-637X/714/1/915.
- Phan, T. D., J. F. Drake, M. A. Shay, F. S. Mozer, and J. P. Eastwood (2007), Evidence for an elongated (> 60 ion skin depths) electron diffusion region during fast magnetic reconnection, *Phys. Rev. Lett.*, *99*, 255,002.
- Phan, T. D., M. A. Shay, J. T. Gosling, M. Fujimoto, J. F. Drake, G. Paschmann, M. Oieroset, J. P. Eastwood, and V. Angelopoulos (2013), Electron bulk heating in magnetic reconnection at Earth’s magnetopause: Dependence on the inflow Alfvén speed and magnetic shear, *Geophys. Res. Lett.*, *40*, 4475–4480, doi:10.1002/grl.50917.
- Phan, T. D., J. F. Drake, M. A. Shay, J. T. Gosling, G. Paschmann, J. P. Eastwood, M. Oieroset, M. Fujimoto, and V. Angelopoulos (2014), Ion bulk heating in magnetic reconnection exhausts at Earth’s magnetopause: Dependence on the inflow Alfvén speed and magnetic shear angle, *Geophys. Res. Lett.*, *41*, 7002–7010, doi:10.1002/2014GL061547.
- Shay, M. A., J. F. Drake, and M. Swisdak (2007), Two-scale structure of the electron dissipation region during collisionless magnetic reconnection, *Phys. Rev. Lett.*, *99*, 155,002.

- Shay, M. A., C. C. Haggerty, T. D. Phan, J. F. Drake, P. A. Cassak, P. Wu, M. Oieroset, M. Swisdak, and K. Malakit (2014), Electron heating during magnetic reconnection: A simulation scaling study, *Physics of Plasmas*, *21*(12), 122902, doi:10.1063/1.4904203.
- Speiser, T. W. (1965), Particle Trajectories in Model Current Sheets, 1, Analytical Solutions, *J. Geophys. Res.*, *70*, 4219–4226, doi:10.1029/JZ070i017p04219.
- Stark, A., W. Fox, J. Egedal, O. Grulke, and T. Klinger (2005), Laser-induced fluorescence measurement of the ion-energy-distribution function in a collisionless reconnection experiment, *Phys. Rev. Lett.*, *95*, 235,005, doi:10.1103/PhysRevLett.95.235005.
- Wygant, J. R., C. A. Cattell, R. Lysak, Y. Song, J. Dombek, J. McFadden, F. S. Mozer, C. W. Carlson, G. Parks, E. A. Lucek, A. Balogh, M. Andre, H. Reme, M. Hesse, and C. Mouikis (2005), Cluster observations of an intense normal component of the electric field at a thin reconnecting current sheet in the tail and its role in the shock-like acceleration of ions fluid into the separatrix region, *J. Geophys. Res.*, *110*, A09,206, doi:10.1029/2004JA010,708.
- Yamada, M., J. Yoo, J. Jara-Almonte, H. Ji, R. M. Kulsrud, and C. E. Myers (2014), Conversion of magnetic energy in the magnetic reconnection layer of a laboratory plasma, *Nature Communications*, *5*, 4774, doi:doi:10.1038/ncomms5774.
- Zeiler, A., D. Biskamp, J. F. Drake, B. N. Rogers, M. A. Shay, and M. Scholer (2002), Three-dimensional particle simulations of collisionless magnetic reconnection, *J. Geophys. Res.*, *107*, 1230, doi:10.1029/2001JA000287.

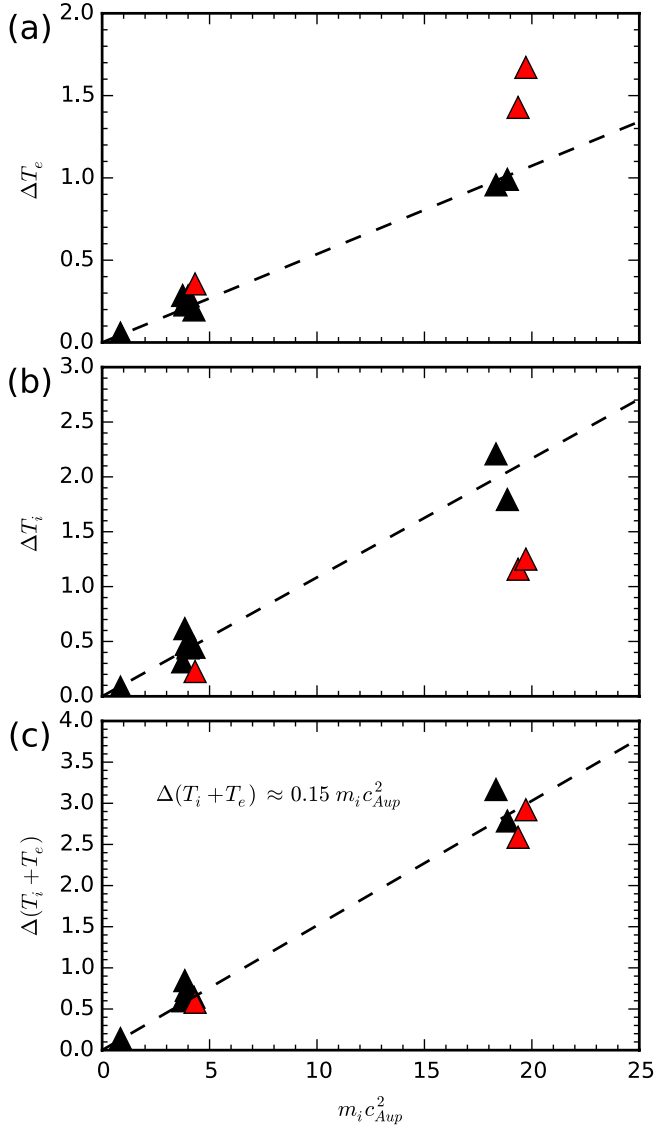


Figure 1. Overview of electron and ion heating: (a) ΔT_e , (b) ΔT_i and (c) $\Delta(T_e + T_i)$ versus $m_i c_{Aup}^2$. The three red triangles have upstream $T_e/T_i = 9$. The change in total temperature appears insensitive to T_{eup} with $\Delta(T_e + T_i) \approx 0.15 m_i c_{Aup}^2$

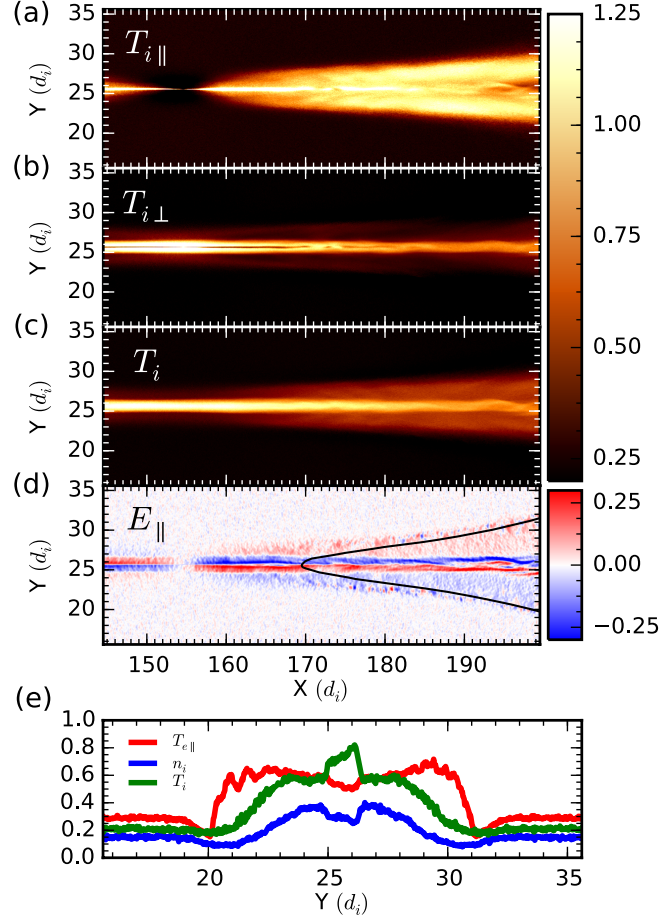


Figure 2. Exhaust structure for a typical simulation with $B = 1.0$, $n = 0.2$, $T_i = T_e = 0.25$, and $m_i/m_e = 100$ (a) $T_{i\parallel}$, (b) $T_{i\perp}$ and (c) T_i using the same color scale; (d) Spatially smoothed E_{\parallel} with single field line in black. Note that the large scale parallel electric field that fills the exhaust, as opposed to the small scale electric field at the midplane, plays a key role in modifying the heating. (e) n , T_i , and $T_{e\parallel}$ along Y at $X = 194.5$.

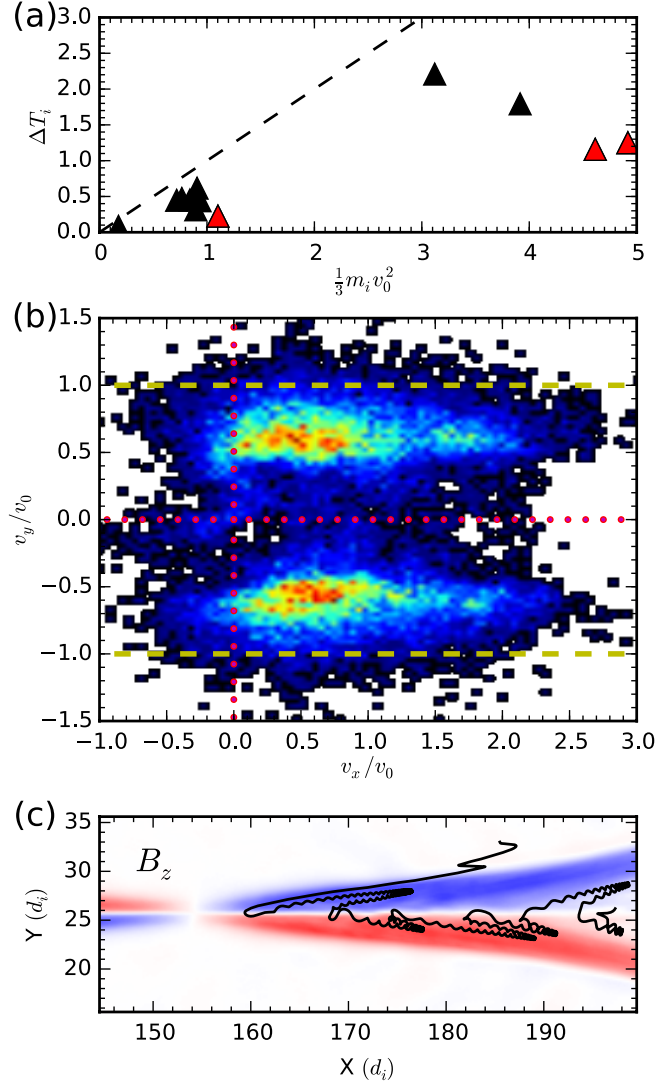


Figure 3. Test of the basic counterstreaming ion model. (a) ΔT_i versus the theoretical prediction $m_i v_0^2/3$ (the dashed line has a slope of 1). The three red triangles have upstream $T_e/T_i = 9$. (b) Ion distribution function around $(X, Y) = (25.6, 190)$ from the simulation in Fig. 2. Velocities are normalized to v_0 (the asymptotic field line velocity), with dotted red lines showing $v_{x,y} = 0$ and dashed yellow lines showing $v_y = v_0$. (c) 2D trajectory of a test particle (electron) entering the reconnection exhaust plotted over B_z . The particle was initialized upstream with the local ExB velocity, and shows the typical trajectory of an electron in the reconnection exhaust. The particle is evolved in the fields from the time averaged simulation using the Boris algorithm.

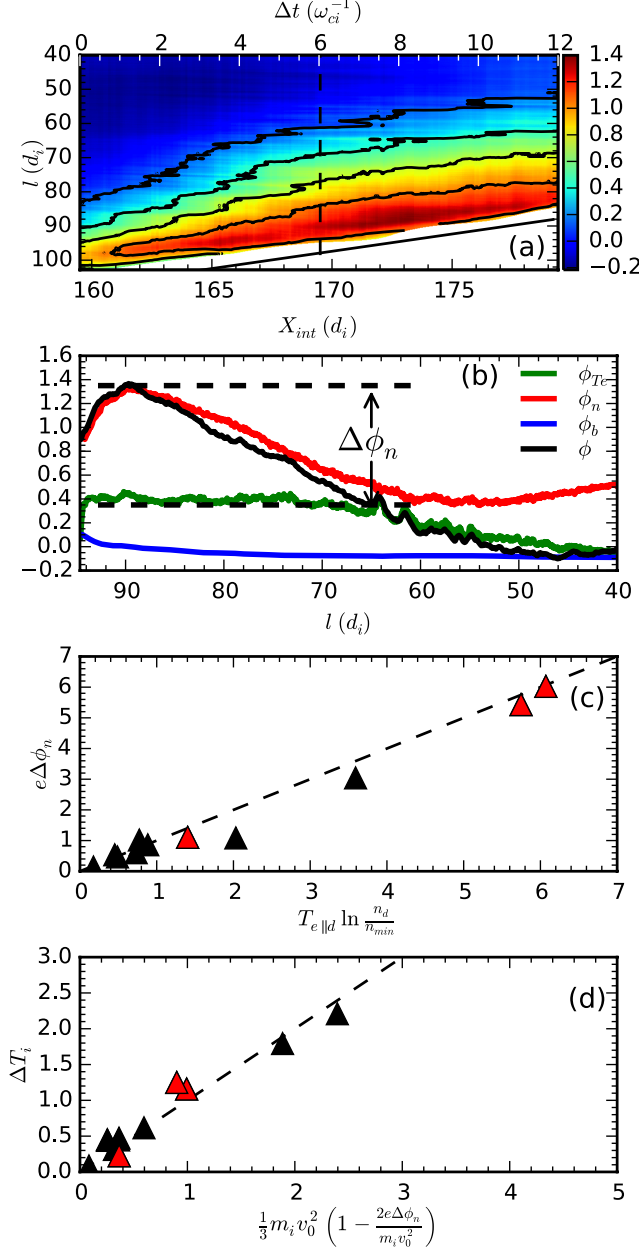


Figure 4. (a) The shortening of field lines in the expanding exhaust and the field-aligned propagation of the spatial variation of ϕ for the same simulation as Fig 2. Shown is ϕ as a function of distance l along a field line (with $l = 0$ at the X value of the middle of the island ($X = 256.9$)) and X_{int} the intercept location of the field line at the midplane of the exhaust. The time axis is defined by $\Delta t = \Delta X_{int}/v_0$ where v_0 is the asymptotic field line velocity. ϕ is taken to be zero at $l = 0$. (b) ϕ , ϕ_{Te} , ϕ_n , and ϕ_B versus l along the solid black magnetic field line in Fig. 2d with $l = 0$ defined as in (a). (c) $e\Delta\phi_n$ versus $T_{e||d} \ln(n_d/n_{min})$. (d) ΔT_i versus the predicted temperature increment including the effect of $\Delta\phi_n$ (Eq. 4).

D R A F T

February 20, 2022, 12:05pm

D R A F T